Colloidal $Ag_2SbBiSe_4$ nanocrystals as *n*-type thermoelectric materials

Bingfei Nan [a, b], Jing Yu [a,c], Mengyao Li [d], Hongyu Chen [e], Hao Zhang [e], Cheng Chang [f], Xuan Song [g], Kai Guo [h *], Jordi Arbiol [c, i], Andreu Cabot [a, i,**]

[a] Catalonia Institute for Energy Research—IREC, Sant Adrià de Besòs, Barcelona 08930, Spain

[b] Universitat de Barcelona, Martí i Franquès 1, 08028, Barcelona, Spain

[c] Catalan Institute of Nanoscience and Nanotechnology (ICN2), Campus UAB, Bellaterra, Barcelona 08193, Catalonia, Spain

[d] Key Laboratory of Material Physics of Ministry of Education, School of Physics and Microelectronics, Zhengzhou University, Zhengzhou 450001, China

[e] School of Information Science and Technology and Department of Optical Science and Engineering and Key Laboratory of Micro and Nano Photonic Structures (MOE), Fudan University, Shanghai, 200433 China

[f] School of Materials Science and Engineering, Beihang University, Beijing 100191, China

[g] The State Key Laboratory of Chemical Engineering, Department of Chemical Engineering, Tsinghua University, Beijing 100084, China

[h] School of Physics and Materials Science, Guangzhou University, Guangzhou, 510006, China

[i] ICREA, Pg. Lluís Companys 23, 08010 Barcelona, Catalonia, Spain

Email: kai.guo@gzhu.edu.cn (K. Guo); acabot@irec.cat (A. Cabot).

Abstract

Materials with low intrinsic thermal conductivity are essential for the development of high-performance thermoelectric devices. At the same time, the solution processing of these materials may enable the cost-effective production of the devices. Herein, we detail a high-yield and scalable colloidal synthesis route to produce $Ag_2SbBiSe_4$ nanocrystals (NCs) using

amine-thiol-Se chemistry. The quaternary chalcogenide material is consolidated by a rapid hot-press maintaining the cubic crystalline structure. Transport measurements confirm that *n*-type $Ag_2SbBiSe_4$ exhibits an inherently ultralow lattice thermal conductivity of ca. 0.34 W $m^{-1}K^{-1}$ at 760 K. Moreover, a modulation doping strategy based on the blending of semiconductor $Ag_2SbBiSe_4$ and metallic Sn NCs is demonstrated to control the charge carrier concentration in the final composite material. The introduction of Sn nanodomains additionally blocks phonon propagation thus contributing to reducing the thermal conductivity of the final material. Ultimately, a peak thermoelectric figure of merit value of 0.64 at 760 K is achieved for *n*-type $Ag_2SbBiSe_4$-Sn nanocomposites that also demonstrate a notable Vickers hardness of 185 HV.

Keywords: Thermoelectricity; quaternary chalcogenide; $Ag_2BiSbSe_4$; nanocrystal; modulation doping; hot press.

1. Introduction

Multinary metal chalcogenides are used in numerous applications such as optoelectronic devices, photovoltaics, photocatalysis and thermoelectrics due to their ample compositional versatility allowing optimization of their chemical and physical properties [1-8]. They are particularly interesting as thermoelectric (TE) material to directly and reversibly convert heat to electricity, thus offering an environment-friendly alternative for power generation and cooling [9-12]. The efficiency of TE materials is generally assessed by a dimensionless figure of merit (*ZT*), $ZT=S^2\sigma T/\kappa_{tot}$, where *S*, σ, *T* and κ_{tot} are the Seebeck coefficient, electrical conductivity, absolute temperature and total thermal conductivity, respectively. Besides, κ_{tot} can be divided into an electronic contribution (κ_{ele}) and a lattice contribution (κ_{lat}); $\kappa_{tot} = \kappa_{ele} + \kappa_{lat}$. The coupling between the electrical and thermal transport properties challenges designing TE materials that reach high *ZT* values. Thus a common approach to maximize ZT is to seek semiconductors with low intrinsic thermal conductivity and then optimize their TE parameters through adjusting the carrier concentrations and electronic structures [13].

While TE materials are generally produced by solid-state approaches at high

temperatures [14-17], nanocrystalline analogues can often be synthesized at much lower temperatures using low-energy wet-chemistry strategies [18-22]. Besides, solution-synthesis methods facilitate a versatile modulation of the material functional properties through precisely controlling composition and size. Thus, solution-based strategies and specifically colloidal synthesis methods are particularly suitable for producing nanocrystal (NC) building blocks for the bottom-up engineering of TE nanomaterials and devices [23-29]. Multinary metal selenide NCs such as $AgSbSe_2$, Cu_3SbSe_4, $NaBi_{1-x}Sb_xSe_2$, Cu_2SnSe_3, $Cu_2ZnGeSe_4$, $Cu_2CdSnSe_4$, and $Cu_2HgGeSe_4$ have been synthesized and consolidated into nanomaterials showing notable TE performances [30-36]. The nanomaterials sintered from these NC building blocks are generally characterized by relatively low intrinsic thermal conductivities and thus are excellent candidates to be doped to optimize performance in different temperature ranges.

Ternary $AgBiSe_2$ and $AgSbSe_2$ are attractive alternatives to Te-based TE materials. Pure $AgBiSe_2$ usually exhibits a complex structural phase transition from a hexagonal to a cubic phase [37]. Pb-doping provides $AgBiSe_2$ with a *p*-type conductivity but at the expense of deteriorating the charge transport performance [38]. $AgBiSe_2$ and $AgBi_{0.5}Sb_{0.5}Se_2$ homojunctions produced via solution-synthesis strategies have been also reported to display p-type performance [39, 40]. However, un-doped $AgBiSe_2$ generally shows an *n*-type conductivity when produced by solid-state processes. In terms of crystal structure, bulk $AgBiSe_2$ displays a cubic phase only at high temperatures, but $AgSb_{0.5}Bi_{0.5}Se_2$ maintains the cubic structure even at room temperature. Another silver pnictogen diselenide, $AgSbSe_2$, is a *p*-type semiconductor that displays a cubic structure with a space group of $Fm\bar{3}m$ at all temperature ranges [13]. The crystallographic and TE properties of $Ag(Bi,Sb)Se_2$ solid solutions with various Sb concentrations have been extensively studied. The Sb solubility limit is in the range of 0.15 to 0.2 for $AgBi_{1-x}Sb_xSe_2$, but these materials are generally unstable during heat cycling processes because of the freezing cubic phases at high temperatures [41]. Sudo et al. reported cubic $AgBi_{0.7}Sb_{0.3}Se_2$ undergoes polymorphic transformation to a hexagonal phase with Nb doping, but it still faces challenges to reach high TE performance [13].

$Ag_2BiSbSe_4$ is another interesting material from the silver pnictogen diselenides family

that has been less intensively studied. Herein, a facile hot injection colloidal synthesis method for the synthesis of $Ag_2SbBiSe_4$ NCs without impurity phases is developed. $Ag_2SbBiSe_4$ NCs serve as building blocks to produce bulk nanomaterials through hot-pressing sintering. Subsequently, the crystalline phase stability and TE properties of the nanomaterial obtained from the consolidation of these NCs are systematically studied. Besides, to improve the TE performance of $Ag_2SbBiSe_4$, a modulation doping strategy based on combining $Ag_2SbBiSe_4$ and Sn NCs is adopted. $Ag_2SbBiSe_4$ nanomaterials show inherently low thermal conductivity and can be regarded as a new and promising TE candidate that can be further optimized.

2. Experimental section

2.1. Chemicals

Silver nitrate ($AgNO_3$, 99.9+%), bismuth(III) acetate ($Bi(OAc)_3$, 99%), antimony(III) chloride ($SbCl_3$, 99.9%), tin(II) chloride ($SnCl_2$, 99%), selenium powder (Se, 99+%), oleylamine (OAm, $C_{18}H_{37}N$, C18-content 80%-90%), oleic acid (OA) and 1-dodecanethiol (1-DDT, 98%) were ordered from Fisher. Unless otherwise stated, all chemicals and reagents were used as received without any additional purification.

2.2. Preparation of selenium precursor stock solution

0.3948 g (5 mmol) of selenium powder, 5 mL of OAm and 5 mL of 1-DDT were loaded into a 50 mL three-neck flask at room temperature, which was then cycled between vacuum and nitrogen to remove the oxygen, and then stirred under a nitrogen atmosphere until Se powder was completely dissolved.

2.3. Synthesis of $Ag_2SbBiSe_4$ NCs

In a typical synthesis, 2.5 mmol of $AgNO_3$ (0.4247 g), 1.25 mmol of $SbCl_3$ (0.2852 g), 1.25 mmol of $Bi(OAc)_3$ (0.4826 g) were loaded into a 250 mL three-neck flask with a mixture of 70 mL of OAm and 10 mL of OA. The solution was magnetically stirred for 30 min at room temperature under a Schlenk line followed by alternately switching to purge with argon and degassing three times. Then, the solution was heated to 130 °C on a heating mantle for an

additional 30 min under vacuum to remove low boiling point impurities. After degassing, the solution was heated to 220 °C at 10 °C/min under an argon atmosphere. Subsequently, upon reaching the set temperature, 10 mL of the Se precursor solution prepared in the previous step was injected into the flask and held for 15 min. Afterwards, the flask was cooled to room temperature by placing it into a cold-water bath. The black product was separated using centrifugation (9000 rpm, 5 min) by adding chloroform for the first time. Afterwards, $Ag_2SbBiSe_4$ NCs in 10 mL of chloroform were precipitated by ethanol ($V_{chloroform:\ ethanol}$=1:2, repeated three times). The centrifuged products were dried under vacuum and kept until their use.

2.4. Blending of NCs

Sn NCs with a diameter of ~12 nm were prepared following a published protocol [42]. $Ag_2SbBiSe_4$-Sn nanocomposites were prepared by mixing $Ag_2SbBiSe_4$ with Sn NCs in solution with Sn mass percentages of 1%, 2% and 3%. A typical procedure involves mixing $Ag_2SbBiSe_4$ and metal NCs in 5 mL of chloroform and then sonicating the mixture for 40 min. Finally, the mixture was dried under vacuum before use.

2.5. Pellet fabrication

The dried fine powders were first annealed in a furnace tube at 450 °C under Ar for 2 h, and then collected into a graphite die and introduced into an argon-filled glovebox for sintering by a hot-press at 500 °C under an axial pressure of 50 MPa for 5 min.

2.6. Characterization

The samples on silicon substrates were tested using a Zeiss Auriga scanning electron microscopy (SEM) equipped with an Oxford energy-dispersive X-ray spectrometer (EDS) working at 15.0 kV. Powder X-ray diffraction (XRD) data were collected on a Bruker AXS D8 Advance X-ray diffractometer with Cu Kα radiation (λ=1.5406 Å) operating at a voltage of 40 kV and current of 40 mA to identify phase and structure. The lattice parameters deduced from the XRD patterns were refined using the Rietveld method in GSAS software with EXPGUI interface [43]. NCs and hot-pressed pellets were analysed by high-resolution transmission electron microscopy (HRTEM) and high-angle annular dark-field (HAADF)

scanning TEM (STEM) in a Tecnai F20 microscope operated at 200 kV. Complementary HAADF STEM and compositional electron dispersive X-ray spectroscopy (EDX) analyses were performed in a Thermo Fisher Spectra 300 microscope operated at 300 keV. The fast Fourier transform (FFT) and inverse fast Fourier transform (IFFT) patterns were acquired from atomic resolution HAADF STEM images obtained in the Spectra 300 aberration-corrected STEM. Ultra-violet–visible (UV−vis) absorption spectroscopy was performed on a UV3150 spectrometer. Ultraviolet photoelectron spectroscopy (UPS) was analysed using a Thermo Scientific K-Alpha system. Thermogravimetric analysis (TGA) and differential scanning calorimetry (DSC) were carried out on a Netzsch DSC at a heating rate of 10 K min^{-1} with an argon gas atmosphere. All polished pellets after hot pressing and sintering have a diameter of ca. 10 mm and a thickness of ca. 1-1.5 mm. Seebeck coefficient (S) and resistivity ($1/\sigma$) were measured by an LSR-3 Linseis platform under a helium atmosphere. Thermal diffusivity was measured on an XFA 600 xenon flash apparatus. The Archimedes' drainage method was adopted to determine the density (ρ) of the materials. Dulong-Petit law was used to calculate specific heat capacity. Hall coefficient measurements were performed on a Hall Effect Analyzer by Linseis Company with a magnetic field of 0.6 T (ezHEMS, NanoMagnetics).

3. Results and discussion

Quaternary $Ag_2SbBiSe_4$ (ASBS) NCs were synthesized in a mixture of OAm and OA using amine-thiol-Se chemistry through a hot-injection synthetic approach (Figure 1a). Silver nitrate, antimony chloride and bismuth acetate were used as Ag^+ Sb^{3+} and Bi^{2+} sources, respectively. The solution was then heated to 220°C under an Ar atmosphere, maintained at this temperature for 15 min, and then rapidly cooled to room temperature. Under these reaction conditions, high batch-to-batch reproducibility and a yield of up to 95% were achieved.

The crystal phase of the synthesized NCs was determined by XRD analysis using Rietveld refinement. As shown in Figure 1b, the XRD pattern of the obtained NCs showed strong and sharp Bragg diffraction peaks, demonstrating excellent crystallinity. All XRD

peaks could be assigned to the face-centred cubic NaCl structure (space group: $Fm\bar{3}m$) of ASBS NCs, which is in good agreement with the standard PDF card 03-065-6177. No XRD peaks of other possible phase impurities in the synthesized product were detected, indicating a phase-pure compound. Figure 1c shows the XRD patterns of ASBS NCs heat-treated in argon atmosphere at different temperatures. No secondary phases were found on the heat-treated samples. The increase in treatment temperature improved the crystallinity of the NCs, which was manifested by narrower and sharper peaks [44]. The schematic diagram of the crystal structure shows that the three cations, Ag, Sb and Bi, in the sample are disordered and randomly occupy the Na sites, whereas the anion Se is located at the Cl sites (Figure 1d). Disordered cations at the same site are expected to lead to reduced thermal conductivity through site scattering mechanisms [45]. Furthermore, the measured elemental composition of ASBS NCs by EDX was 2.2:1.0:1.1:4 (Figure S1), which was close to the expected Ag:Sb:Bi:Se ratio of 2:1:1:4.

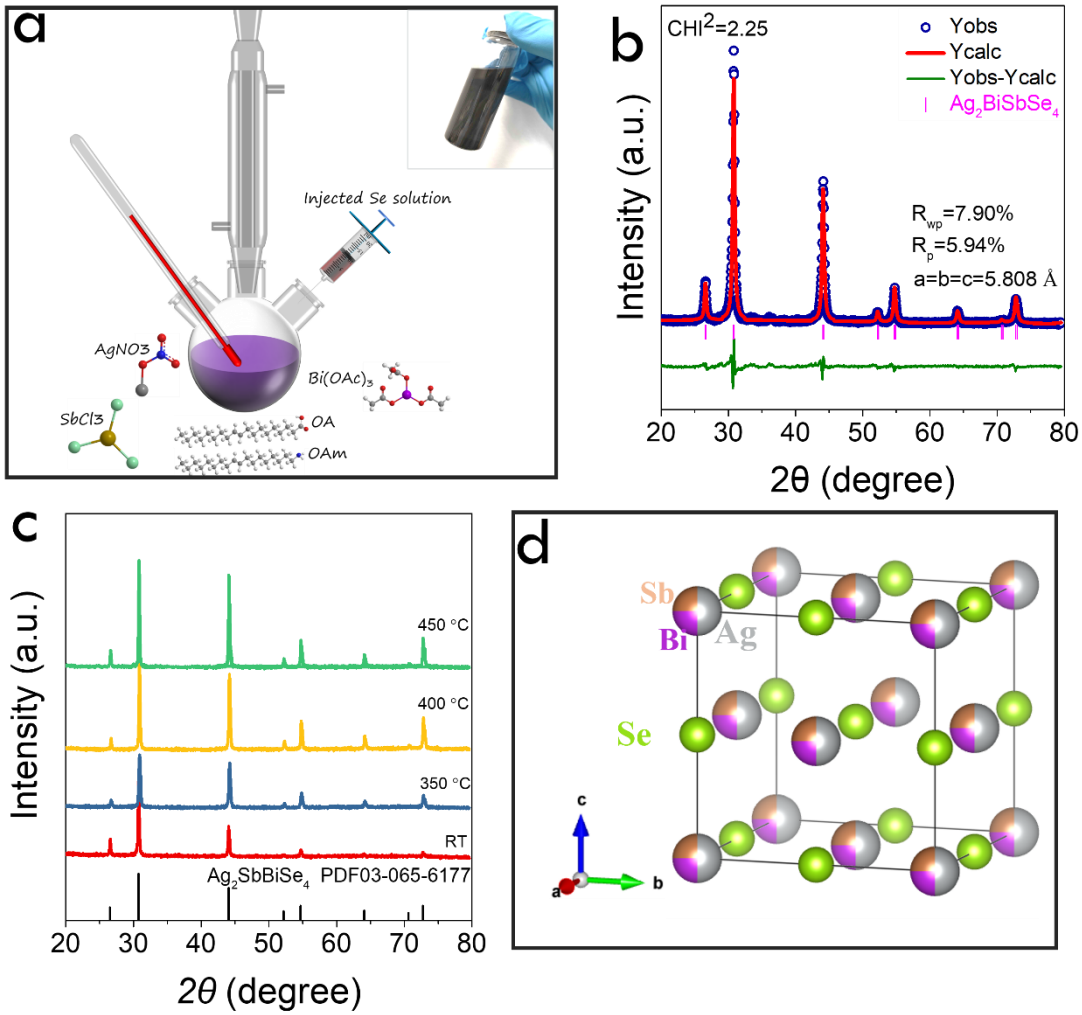

Figure 1. (a) Schematic diagram of the synthesis of quaternary ASBS NCs. The upper right inset shows a glass vial containing ASBS NCs dispersed in hexane. (b) Rietveld refinement of the powder XRD patterns of ASBS NCs. (c) XRD pattern of ASBS NCs thermally annealed at different temperatures. (d) Crystal structure of cubic ASBS NCs with the space group $Fm\bar{3}m$.

Figures 2a and b show HRTEM micrographs of the ASBS NCs. The lattice fringes from the crystalline domain can be clearly observed, confirming that the ASBS NCs had good crystallinity. The characteristic lattice fringe distance was 0.307 nm, which matches the (200) planes of the cubic ASBS phase (Figure 2b). TEM and high-angle annular dark-field imaging (HAADF) micrographs showed the average size of ASBS was around 9.5±1.3 nm and the particle geometry was quasi-spherical (Figures 2c and S2). Through the HAADF micrograph and corresponding EDS mappings, it is evident that the ASBS NCs were composed of 4

elements: Ag, Sb, Bi, Se, that were uniformly distributed without any signs of segregation (Figure 2d-i).

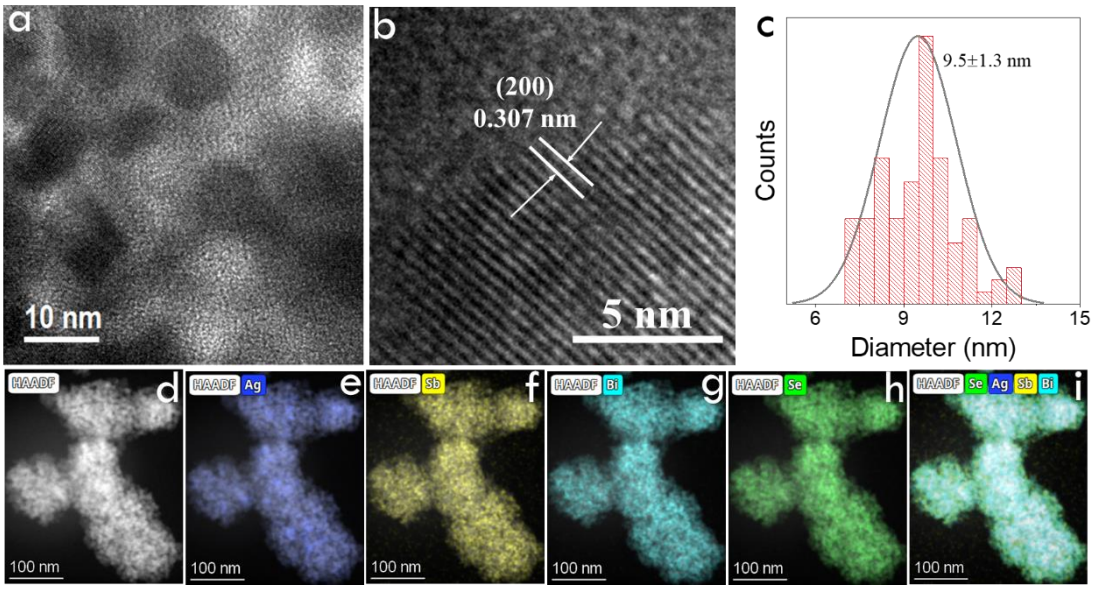

Figure 2. (a,b) Representative HRTEM micrographs of ASBS NCs. (c) Size distribution of the obtained NCs. (d) HAADF STEM micrograph and (e-i) corresponding EDX compositional maps for Ag, Sb, Bi, and Se of ASBS NCs.

The absorption coefficient and optical properties of the ASBS NCs were determined using UV-vis spectroscopy at room temperature. As can be seen in Figure 3a, ASBS NCs exhibited broad absorption in the wavelength ranges from the visible to the near-infrared regions. The direct bandgap (E_g) of ASBS was estimated at ca. 1.62 eV as evaluated by plotting a Tauc plot of the absorption coefficient as a function of photon energy ($h\nu$). The E_g of quaternary ASBS was significantly larger compared with narrow bandgap TE materials such as Ag_2Se (0.19 eV) [46], PbSe (~0.28 eV) [47], Bi_2Te_3 (0.16 eV) [48], but it was close to the bandgap value reported for several other quaternary systems, e.g. 1.54 eV for $AgInSnS_4$ [1], 1.51-1.57 eV for $AgBaGeSe_4$ [49], 1.4 eV for $Ag_2ZnSnSe_4$ [50], and 1.54 eV for $Cu_3InSnSe_5$ [51]. These relatively wide bandgap semiconductors generally show poorer electrical transport properties.

The thermal stability of the ASBS sintered pellets was evaluated using TGA and DSC measurements (Figure 3b). The TGA curve shows that the ASBS nanomaterial was thermally stable at temperatures up to 700 °C with less than 2.1 % weight loss. At the same time, no

obvious peaks were observed in the range from room temperature to 700 K in the DSC curve.

As shown in Figure 3c, the largely negative Seebeck coefficient (*S*) values demonstrated the n-type character of ASBS. Although ASBS nanomaterials possessed high absolute *S* values, relatively low electrical conductivities (σ) of 1.6×10^3 S m^{-1} at 760 K limited the TE performance of the intrinsic ASBS nanomaterial. This poor σ of the ASBS pellet was mainly related to a relatively low charge carrier mobility and an insufficient charge carrier concentration (*n*). The intrinsic Hall carrier concentration of pure ASBS was determined to be 1.5×10^{18} cm^{-3} at room temperature, which was lower than that of similar TE materials such as $AgBiSe_2$ (5.85×10^{18} cm^{-3} [52]) and $AgSbSe_2$ (8×10^{18} cm^{-3} [53]). Besides, as shown in Figure 3d, the temperature-dependence of the total thermal conductivity (κ_{tot}) showed low κ_{tot} values ranging from 0.47 W m^{-1}K^{-1} at room temperature to 0.36 W m^{-1}K^{-1} at 760 K. As a result, the ASBS nanomaterial achieved a maximum *ZT* of 0.28 at 760 K.

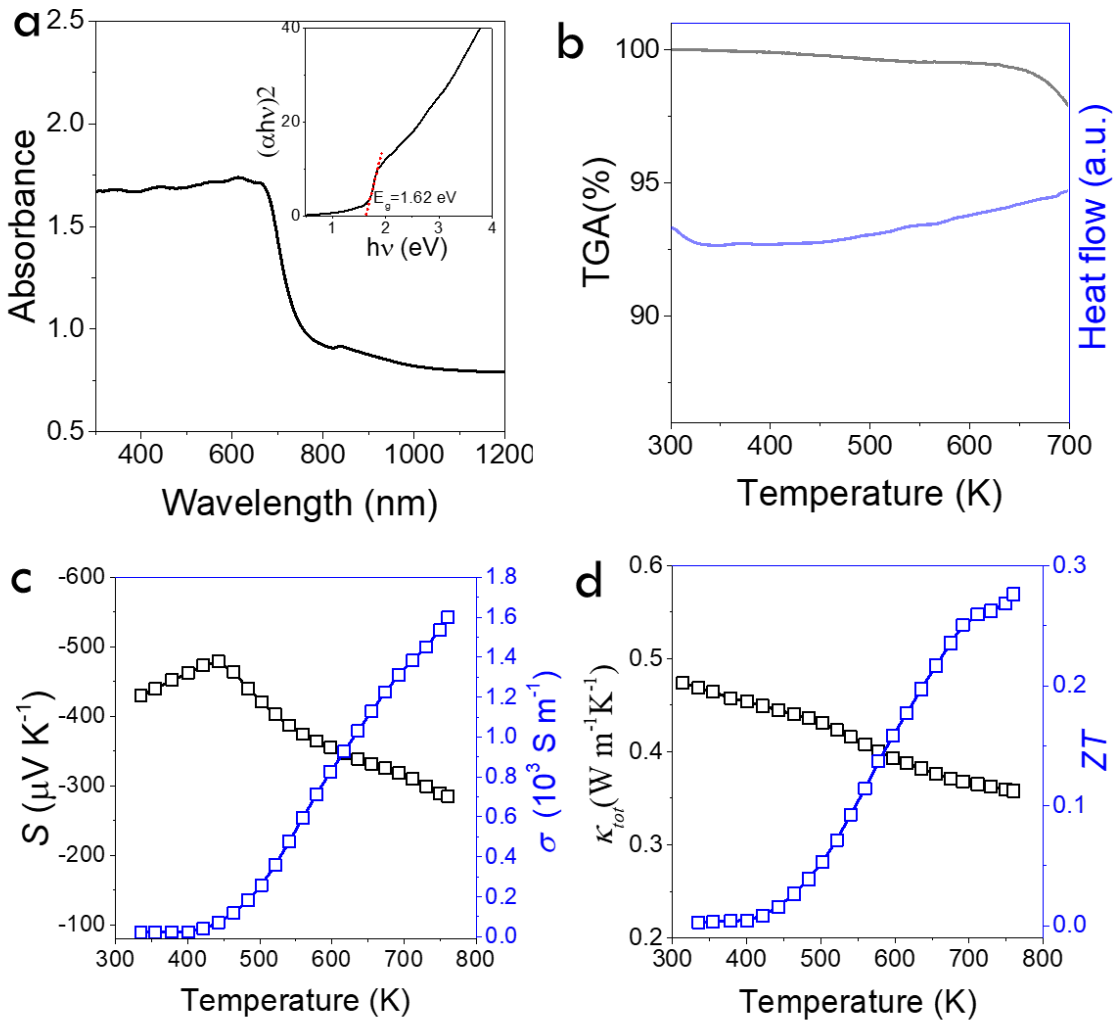

Figure 3. (a) UV-vis absorption spectrum and the inset of corresponding Tauc plot extrapolated to estimate a direct optical bandgap from the UV−vis absorption spectrum of ASBS nanomaterials (where α is optical absorption coefficient, h is Planck's constant, and v is photon frequency [54]). (b) Temperature dependence TGA and DSC curves of ASBS nanomaterials from 300 to 700 K. (c) Seebeck coefficient (S) and electrical conductivity (σ) of the ASBS nanomaterial. (d) Total thermal conductivity (κ_{tot}) and figure of merit (ZT) values of the ASBS nanomaterial.

To overcome the limitation of the poor electrical properties of the intrinsic ASBS, metallic Sn NCs were incorporated into the matrix. The combination of n-type semiconductor materials with a low work function metal allowed injecting electrons into the semiconductor, thus controlling the charge carrier concentration with minimal influence on mobility [55-57]. The charge injection nanodomains can be easily introduced during the bottom-up assembly of colloidal NCs, thus opening a convenient door to modulated doping and comprehensively optimising the TE properties of semiconductor materials [23]. Additionally, metal ions can be introduced within the semiconductor material in the process, further enhancing the doping effect. ASBS-Sn nanocomposites were produced by combining the as-synthesized ASBS NCs with Sn NCs in hexane and then evaporating the solvent. The obtained blends were annealed in a furnace under an argon atmosphere to remove organic residues. Then the annealed powder was hot-pressed into ASBS-Sn nanocomposite pellets with ca. 10 mm in diameter and ca. 1 mm in thickness. The macroscopic pellets showed metallic lustre (Figure 4b).

The phase purity and crystal structure of the sintered ASBS-Sn nanocomposites were first confirmed by XRD analysis (Figure 4a). All peaks of the Sn-doped samples could be attributed to the cubic structure without second phases within the limit of detection. Additionally, the Bragg peaks shifted to a lower angle, and the lattice constant parameters gradually increased with the amount of Sn NCs. This is associated with the introduction of Sn^{2+} ions within the ASBS lattice, since Sn^{2+} (1.18 Å) has a larger ion radius than Ag^{+} (1.15 Å), Sb^{3+} (0.76 Å) and Bi^{3+} (1.03 Å) (Figure 4b) [58, 59]. The small amount of Sn introduced did not allow for observing the XRD pattern of the metallic Sn.

SEM images of the annealed ASBS-Sn nanocomposite powders are shown in Figure S3, and the EDS composition for ASBS-Sn nanocomposite pellets is displayed in Table S1.

Figures 4c-d show the microscopic morphologies of fractured pellets as analysed by SEM. After consolidation of the ASBS-Sn nanocomposites, NCs coalesced and grew into larger particles with sizes ranging from nanometers to micrometres. Figure 4e depicts a HAADF STEM image and the corresponding electron energy loss spectroscopy (EELS) elemental maps of an ASBS-Sn nanocomposite. Compared with the relatively uniform distribution of Ag, Sb, Bi and Se in the nanocomposite matrix, Sn presented a much less homogeneous distribution, with some Sn segregated areas. EDX elemental maps demonstrated similar results with some Sn high-concentration spots (Figure S4). Figure 4f depicts a HAADF STEM image showing a grain boundary within the nanocomposite and multiple dislocations as observed through the IFFT image (Figure 4g). In addition, as shown in Figure 4h, a geometrical phase analysis (GPA) using the Fourier transform to generate strain maps, displayed notable strain fields throughout the nanocrystalline domains due to the lattice mismatch at the interface, which induced the formation of misfit dislocations. The large density of Sn nanodomains, grain boundaries, dislocations, and strain fields are expected to increase phonon scattering, thereby reducing the lattice thermal conductivity, as will be discussed later.

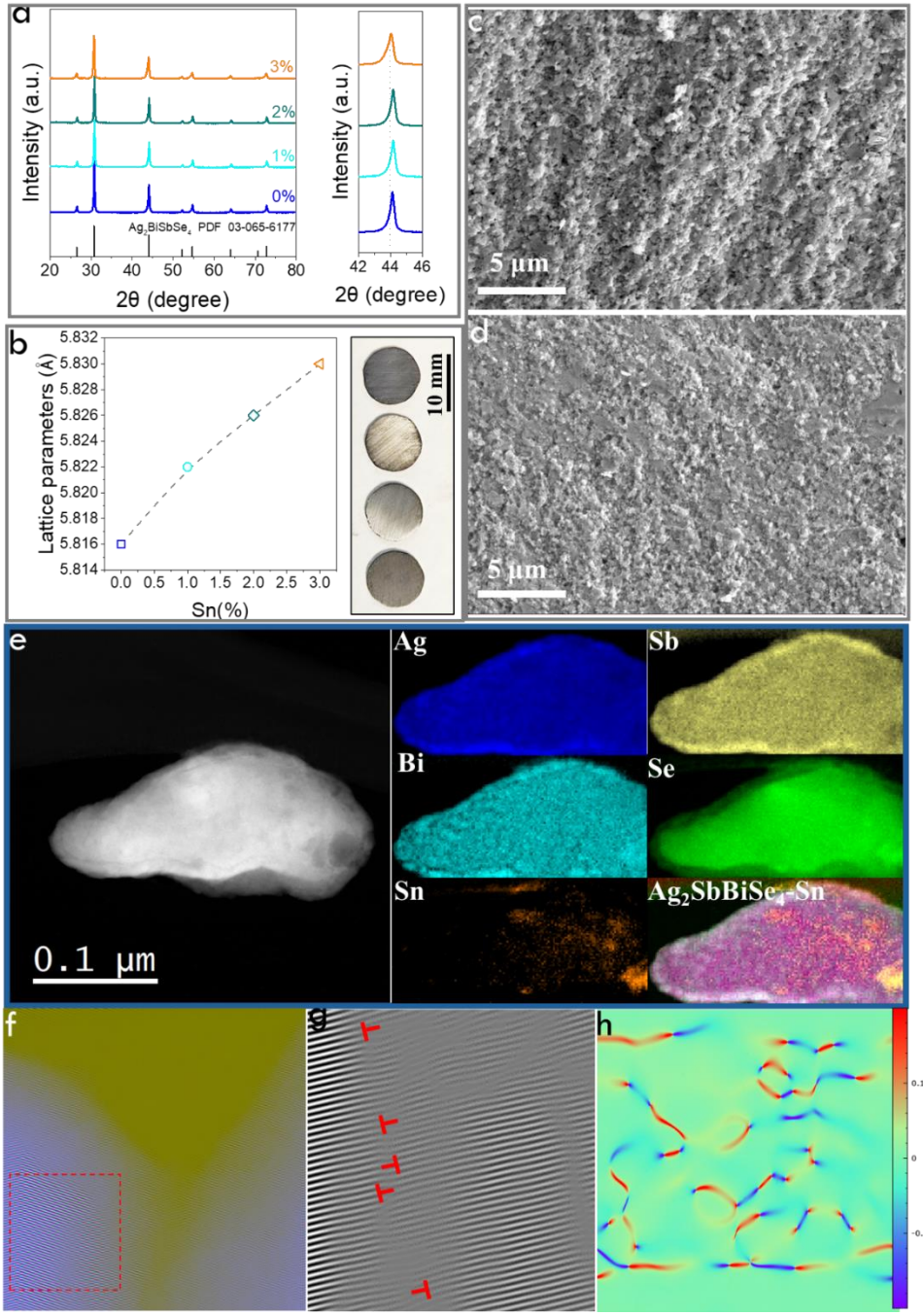

Figure 4. (a) XRD patterns of all ASBS-Sn nanocomposites including the reference pattern ($Ag_2SbBiSe_4$ PDF 03-065-6177) and (b) corresponding calculated lattice parameters of ASBS-Sn nanocomposites. (c-d) Representative SEM images of the fractured surface obtained from ASBS-Sn nanocomposites with (c) ASBS, and (d) ASBS-2%Sn. (e) HAADF STEM image and corresponding EELS chemical composition maps for Ag, Sb, Bi, Se and Sn. (f) HAADF STEM micrograph of a grain boundary. (g) IFFT image showing dislocations from a selected area in (f). (h) GPA strain analysis along the ϵ_{yy} direction.

As shown in Figure 5a, the σ of ASBS-Sn nanocomposites increased with the Sn content throughout the entire temperature range. For ASBS-2%Sn, the highest σ value of 6.48×10^3 S m^{-1} was obtained at 760 K. The increase of σ with temperature denotes a semiconducting transport behaviour. The σ enhancement is mainly attributed to the increased charge carrier concentration (Figure 5b). The n_H of ASBS-1%Sn, ASBS-2%Sn and ASBS-3%Sn at room temperature were 2.35×10^{18} cm^{-3}, 5.45×10^{18} cm^{-3} and 1.04×10^{19} cm^{-3}, respectively. The introduction of Sn obviously improved the n_H, which is consistent with previous reports [56, 60]. In addition, the Hall mobility (μ_H) of ASBS-Sn nanocomposites also showed a slight enhancement, which points to a modulation doping strategy as the main responsible for the increased charge carrier concentration (Table S2).

The ASBS-Sn nanocomposite exhibited negative *S* values over the entire measured temperature range, with an overall decrease in absolute *S* values as the Sn concentration increased (Figure 5c). *S* and *n* are proven to be inversely proportional according to the relationship of $S\sim n^{-2/3}$ in the Mott-Jones formula, [52]. Therefore, the decrease in *S* in the modulation-doped ASBS nanocomposites is assigned to the increased n_H.

The temperature dependence of the power factor ($PF=\sigma S^2$) of all nanocomposites calculated from the measured σ and *S* is shown in Figure 5d. The *PF* of composite samples showed obvious improvement compared with the pristine ASBS nanomaterial. The ASBS-2%Sn nanocomposite exhibited the largest *PF* at 0.30 mW m^{-1} K^{-2} at 760 K, which was 2.3 times that of pure ASBS nanomaterials.

A work function value of 6.04 eV was measured for the ASBS nanocomposite by UPS (Figure S5), which was higher than that of Sn (4.42 eV). Thus electrons from Sn can spill off to the ASBS phase, thereby increasing the σ of the ASBS-Sn nanocomposites with respect to ASBS (Figure 5e) [61, 62].

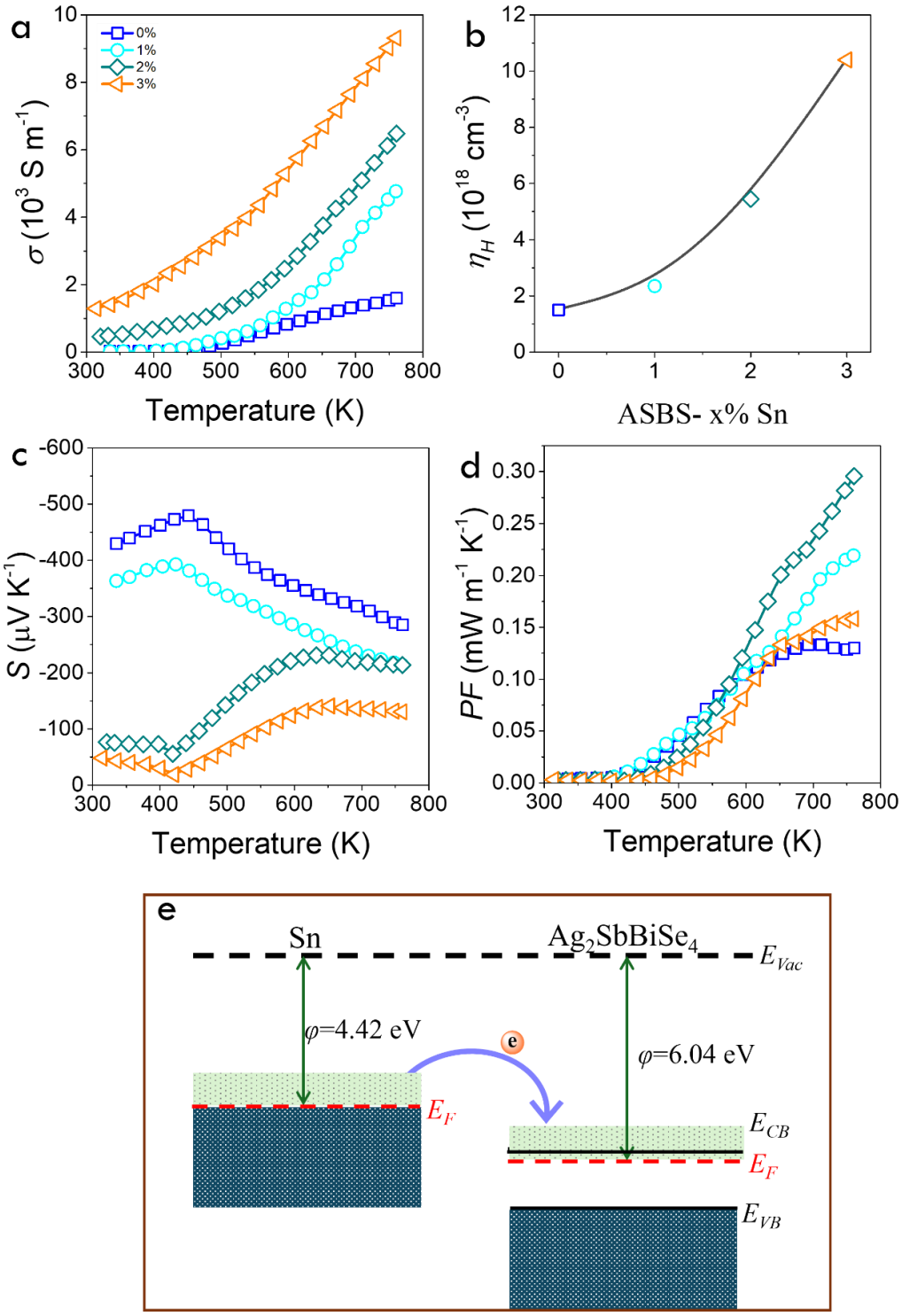

Figure 5. Transport properties of ASBS-Sn pellets. (a) Temperature dependence of the electrical conductivity (σ). (b) Room-temperature Hall carrier concentration (n_H). (c,d) Temperature dependence of the Seebeck coefficient (S) and power factor ($PF=\sigma S^2$). (e) Energy band diagram of the interface of Sn nanodomains and the ASBS matrix before and after contact: E_{vac} is the vacuum level, E_{CB} is the energy of the minimum of the conduction band, E_{VB} is the energy of the maximum of the valence band, and E_F is the Fermi level.

Figure 6a displays the temperature dependence of κ_{tot} from the ASBS-Sn nanocomposites. At room temperature, the introduction of Sn reduced the κ_{tot} from 0.47 W m^{-1} K^{-1} for pristine ASBS to ca. 0.45 W m^{-1} K^{-1} at a concentration of 1–2%Sn. The lattice thermal conductivity (κ_{lat}) was estimated directly by subtracting the electronic contribution (κ_{ele}) from the κ_{tot} (i.e., $\kappa_{tot}=\kappa_{lat}+\kappa_{ele}$). Here, κ_{ele} was estimated according to the Wiedemann-Franz law $\kappa_{ele}= L\sigma T$, in which L is the Lorentz number and can be calculated from the corresponding Seebeck coefficient: $L=1.5+exp[-|S|/116]$. Both κ_{ele} and L are shown in Figure S6. As temperature increased, the κ_{lat} of all samples decreased (Figure 6b), reaching down to 0.27 W m^{-1} K^{-1} for the ASBS-2%Sn nanocomposite at 760 K. This value is one of the lowest reported for this system (Figure 6c).

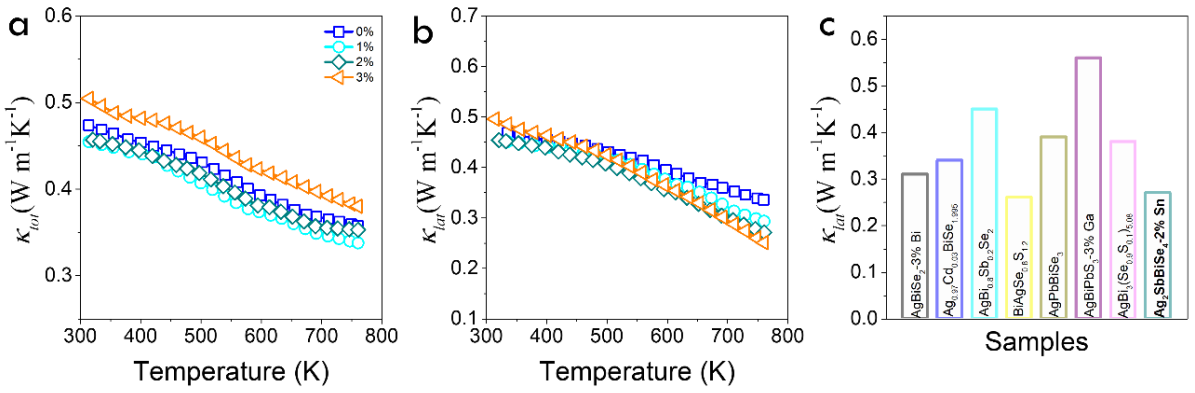

Figure 6. (a,b) Temperature dependence of (a) total thermal conductivity (κ_{tot}) and (b) lattice thermal conductivity (κ_{lat}). (c) κ_{lat} of ASBS-2%Sn nanocomposites and other *n*-type Ag-based multinary chalcogenides reported in the previous literature [45, 63-68].

The temperature dependence of *ZT* calculated from the electrical and thermal transport data for pristine ASBS nanomaterials and all nanocomposites is shown in Figure 7a. A peak *ZT* value of 0.64 at 760 K was obtained for the ASBS-2%Sn nanocomposite, which is ~230% higher than that of the pristine ASBS. Figure 7b and Table 1 compare the performance of ASBS nanomaterials with several previously reported multinary Ag-based chalcogenide TE systems. ZT values of ASBS-Sn nanocomposites at high temperatures are higher than that of previously reported *n*-type Ag-based quaternary TE materials [13, 45, 65, 66, 69, 70] although much room for further optimization is left. Figure S7 displays the TE properties of an ASBS-

2%Sn nanocomposite measured over three cycles, showing good stability and reproducibility.

Apart from optimizing TE properties, it is also essential to ensure that the mechanical properties of the TE material meet the minimum standards required for practical applications [71, 72], which is not straightforward with all materials [73]. As shown in Figure 7c, the Vickers hardness of ASBS was 185.03 HV. The introduction of a small amount of Sn did not seriously deteriorate the Vickers hardness of the ASBS pellet. The ASBS-2%Sn pellet exhibited just a slightly lower Vickers hardness of 184.7 HV, which is still significantly superior or comparable to those of typical Ag-based TE materials with strengthened mechanical performance, such as Ag_2Se [74], $AgSbSe_2$ [74], Ag_8SiSe_6 [75], $AgBiPbSe_2S$ [69], and $AgBiSe_2$ [76], etc. ASBS-2%Sn also has significant mechanical advantages compared with conventional Bi_2Te_3-based materials currently used in commercial TE devices (e.g. 131.5 HV for pure Bi_2Te_3 [77]).

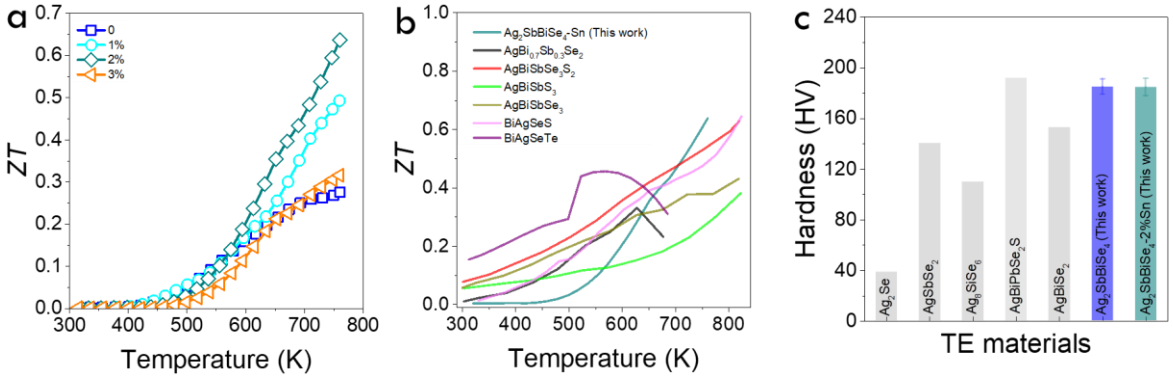

Figure 7. (a) Temperature dependence of the TE figure of merit (*ZT*) of ASBS-Sn nanocomposites. (b) Comparison of the temperature dependence of the *ZT* values of ASBS-2%Sn nanocomposites with other *n*-type Ag-based multinary chalcogenide materials reported in the previous literature [13, 45, 65, 66, 69, 70]. (c) Vickers hardness of ASBS and ASBS-2%Sn pellets compared with those of previously reported Ag-based TE materials.

Table 1. TE performance of different multinary *n*-type Ag-based chalcogenides (some data are estimated from literature figures).

Materials & Refs	$\|S\|_{max}$ ($\mu V\ K^{-1}$)	σ_{max} ($S\ m^{-1}$)	$(\kappa_{tot})_{min}$ ($W\ m^{-1}K^{-1}$)	ZT max

$AgBiSe_2$-3% Bi [63]	-160	~4.35×10^3	~0.67	~0.53@800 K
$AgPbBiSe_3$[45]	-204	7.20×10^3	~0.46	0.43@818 K
BiAgSeS [65]	~-269.64	19 685	~0.47	~0.65@823 K
$BiAgSe_{0.8}S_{1.2}$ [65]	~-744.82	14187	~0.36	~0.6@823 K
$AgBiS_2$ [78]	~-195	~5.2×10^3	~0.43	~0.2@810 K
$AgBiS_{1.92}Se_{0.08}$ [78]	~-104.72	3.10×10^4	~0.75	~0.23@705 K
BiAgSeTe [70]	-190	4.15×10^4	0.72	~0.42@550 K
$AgBiPbS_3$ [66]	~-338.22	~6.16×10^3	~0.60	0.38@823 K
$AgBiPbS_3$-3% Ga [66]	~-244.05	1×10^4	~0.70	~0.4@823
$Ag_{0.97}Cd_{0.03}BiSe_{1.995}$ [64]	-215.62	~7.58×10^3	~0.55	~0.65@773 K
$AgBi_3(Se_{0.9}S_{0.1})_{5.08}$ [67]	~-211.84	1.30×10^4	0.45	0.42@723 K
$Ag_2SbBiSe_4$-2% Sn [this work]	**-231.11**	**6.5×10^3**	**0.35**	**0.64@760 K**

4. Conclusion

In summary, we reported the synthesis of ASBS colloidal NCs with a stable rock-salt structure and investigated their *n*-type TE properties after annealing and subsequent hot-pressing processes. The XRD and microstructure analysis identified uniformly distributed elements within a single-phase ASBS compound. Pristine ASBS pellets showed inherent low thermal conductivity. Additionally, Sn was further employed to modulate the charge carrier concentration and TE performance of ASBS while also reducing the lattice thermal conductivity. ASBS-Sn nanocomposites showed a maximum power factor of 0.30 mW $m^{-1}K^{-2}$ and ZT of 0.64 at 760 K, which was approximately 230% higher than that of undoped ASBS. Furthermore, the mechanical analysis showed ASBS-based materials to be a competitive candidate for implementation in TE materials and devices.

CRediT authorship contribution statement

Bingfei Nan designed and carried out experiments and wrote the first version of the manuscript. Jing Yu, Mengyao Li, Cheng Chang, Hongyu Chen, Hao Zhang, Xuan Song performed characterization of materials. Kai Guo, and Jordi Arbiol performed characterization of materials, analysed the obtained data and helped revising the manuscript. Andreu Cabot provided funding and revised all versions of the manuscript.

Declaration of Competing Interest

The authors declare no competing financial interest.

Acknowledgments

B.F.N. thanks the China Scholarship Council (CSC) for the scholarship support and acknowledges funding from the FWF “Lise Meitner Fellowship” grant agreement M 2889-N. J. Y. thanks the China Scholarship Council (CSC) for the scholarship support. We acknowledge funding from Generalitat de Catalunya 2021SGR00457 and 2021SGR01581. This study is part of the Advanced Materials programme and was supported by MCIN with funding from European Union NextGenerationEU (PRTR-C17.I1) and by Generalitat de Catalunya. ICN2 is supported by the Severo Ochoa program from Spanish MCIN/AEI (Grant No.: CEX2021-001214-S) and is funded by the CERCA Programme/Generalitat de Catalunya. ICN2 is founding member of e-DREAM. [79]. Authors acknowledge the use of instrumentation as well as the technical advice provided by the Joint Electron Microscopy Center at ALBA (JEMCA). ICN2 acknowledges funding from Grant IU16-014206 (METCAM-FIB) funded by the European Union through the European Regional Development Fund (ERDF), with the support of the Ministry of Research and Universities, Generalitat de Catalunya. Part of the present work has been performed in the framework of Universitat Autònoma de Barcelona Materials Science PhD program.

Appendix A. Supplementary data

Supplementary data associated with this article can be found in the online version at XXX.

References

[1] Q. Bian, S. Lei, K. Zhao, Q. Tu, L. Zhao, L. Rao, Y. Xiao, B. Cheng, Isomorphous Substitution Synthesis and Photoelectric Properties of Spinel $AgInSnS_4$ Nanosheets, Chem. Mater. 32(22) (2020) 9713-9720.

[2] L. Wu, Q. Wang, T.-T. Zhuang, G.-Z. Zhang, Y. Li, H.-H. Li, F.-J. Fan, S.-H. Yu, A library of polytypic copper-based quaternary sulfide nanocrystals enables efficient solar-to-hydrogen conversion, Nat. Commun.

13(1) (2022) 5414.

[3] Y. Zhao, M. Liu, W. Zhang, X. Sun, W. Wang, W. Zhang, M. Tang, W. Ren, M. Sun, W. Feng, W. Wang, Solution-phase controlled synthesis of Cu_3NbSe_4 nanocrystals for optoelectronic applications, Dalton Trans. 51(44) (2022) 16937-16944.

[4] C. Wang, G. Ding, The promising thermoelectric performance of newly synthesized bulk $SrCu_2GeSe_4$ and $BaCu_2SnSe_4$ associated with superior band degeneracy, Appl. Phys. Express 14(4) (2021) 045502.

[5] Y. Sun, H. Wang, J. Yao, F. Mehmood, C. Tan, L. Wang, J. Zhai, H. Wang, C. Wang, High symmetry structure and large strain field fluctuation lead enhancement of thermoelectric performance of quaternary alloys by tuning configurational entropy, Chem. Eng. J. 462 (2023) 142185.

[6] D. Quarta, S. Toso, A. Fieramosca, L. Dominici, R. Caliandro, A. Moliterni, D.M. Tobaldi, G. Saleh, I. Gushchina, R. Brescia, M. Prato, I. Infante, A. Cola, C. Giannini, L. Manna, G. Gigli, C. Giansante, Direct Band Gap Chalcohalide Semiconductors: Quaternary $AgBiSCl_2$ Nanocrystals, Chem. Mater. 35(23) (2023) 9900-9906.

[7] F.-J. Fan, L. Wu, S.-H. Yu, Energetic I–III–VI_2 and I_2–II–IV–VI_4 nanocrystals: synthesis, photovoltaic and thermoelectric applications, Energy Environ. Sci. 7(1) (2014) 190-208.

[8] M.D. Regulacio, M.-Y. Han, Multinary I-III-VI_2 and I_2-II-IV-VI_4 Semiconductor Nanostructures for Photocatalytic Applications, Acc. Chem. Res. 49(3) (2016) 511-519.

[9] B. Qin, D. Wang, X. Liu, Y. Qin, J.-F. Dong, J. Luo, J.-W. Li, W. Liu, G. Tan, X. Tang, J.-F. Li, J. He, L.-D. Zhao, Power generation and thermoelectric cooling enabled by momentum and energy multiband alignments, Science 373(6554) (2021) 556-561.

[10] H. Zhu, W. Li, A. Nozariasbmarz, N. Liu, Y. Zhang, S. Priya, B. Poudel, Half-Heusler alloys as emerging high power density thermoelectric cooling materials, Nat. Commun. 14(1) (2023) 3300.

[11] D. Liu, D. Wang, T. Hong, Z. Wang, Y. Wang, Y. Qin, L. Su, T. Yang, X. Gao, Z. Ge, B. Qin, L.-D. Zhao, Lattice plainification advances highly effective SnSe crystalline thermoelectrics, Science 380(6647) (2023) 841-846.

[12] J. Mao, H. Zhu, Z. Ding, Z. Liu, G.A. Gamage, G. Chen, Z. Ren, High thermoelectric cooling performance of n-type Mg_3Bi_2-based materials, Science 365(6452) (2019) 495-498.

[13] K. Sudo, Y. Goto, R. Sogabe, K. Hoshi, A. Miura, C. Moriyoshi, Y. Kuroiwa, Y. Mizuguchi, Doping-Induced Polymorph and Carrier Polarity Changes in Thermoelectric $Ag(Bi,Sb)Se_2$ Solid Solution, Inorg. Chem. 58(11) (2019) 7628-7633.

[14] M. Jin, S. Lin, W. Li, Z. Chen, R. Li, X. Wang, Y. Chen, Y. Pei, Fabrication and Thermoelectric Properties of Single-Crystal Argyrodite Ag_8SnSe_6, Chem. Mater. 31(7) (2019) 2603-2610.

[15] D. Zhang, X. Wang, H. Wu, Y. Huang, S. Zheng, B. Zhang, H. Fu, Z. Cheng, P. Jiang, G. Han, G. Wang, X. Zhou, X. Lu, High Thermoelectric Performance in Earth-Abundant Cu_3SbS_4 by Promoting Doping Efficiency via Rational Vacancy Design, Adv. Funct. Mater. 33(15) (2023) 2214163.

[16] A. Nagaoka, K. Yoshino, T. Masuda, T.D. Sparks, M.A. Scarpulla, K. Nishioka, Environmentally friendly thermoelectric sulphide Cu_2ZnSnS_4 single crystals achieving a 1.6 dimensionless figure of merit ZT, J. Mater. Chem. A 9 (2021) 15595-15604.

[17] H. Chen, C. Shao, S. Huang, Z. Gao, H. Huang, Z. Pan, K. Zhao, P. Qiu, T.-R. Wei, X. Shi, High-Entropy Cubic Pseudo-Ternary Ag_2(S, Se, Te) Materials With Excellent Ductility and Thermoelectric Performance, Adv. Energy Mater. 14(10) (2024) 2303473.

[18] X. Wang, C. Liu, J. Chen, L. Miao, S. Wu, X. Wang, Z. Xie, W. Xu, Q. Chen, Synergistically optimizing the thermoelectric properties of polycrystalline Ag_8SnSe_6 by introducing additional Sn, CrystEngComm 22(2) (2020) 248-256.

[19] T. Nakada, M. Takahashi, C. Shijimaya, K. Higashimine, W. Zhou, P. Dwivedi, M. Ohta, H. Takida, T.

Akatsuka, M. Miyata, S. Maenosono, Gram-Scale Synthesis of Tetrahedrite Nanoparticles and Their Thermoelectric Properties, Langmuir 35(49) (2019) 16335-16340.

[20] H. Yang, L.A. Jauregui, G. Zhang, Y.P. Chen, Y. Wu, Nontoxic and Abundant Copper Zinc Tin Sulfide Nanocrystals for Potential High-Temperature Thermoelectric Energy Harvesting, Nano Lett. 12(2) (2012) 540-545.

[21] B. Nan, M. Li, Y. Zhang, K. Xiao, K.H. Lim, C. Chang, X. Han, Y. Zuo, J. Li, J. Arbiol, J. Llorca, M. Ibáñez, A. Cabot, Engineering of Thermoelectric Composites Based on Silver Selenide in Aqueous Solution and Ambient Temperature, ACS Appl. Electron. Mater. (2023).

[22] M. Li, X. Zhao, D. Wang, X. Han, D. Yang, B. Wu, H. Song, M. Jia, Y. Liu, J. Arbiol, A. Cabot, Enhancing the Thermoelectric and Mechanical Properties of p-Type PbS through Band Convergence and Microstructure Regulation, Nano Lett. 24(26) (2024) 8126-8133.

[23] S. Ortega, M. Ibáñez, Y. Liu, Y. Zhang, M.V. Kovalenko, D. Cadavid, A. Cabot, Bottom-up engineering of thermoelectric nanomaterials and devices from solution-processed nanoparticle building blocks, Chem. Soc. Rev. 46(12) (2017) 3510-3528.

[24] Q. Zhu, S. Wang, X. Wang, A. Suwardi, M.H. Chua, X.Y.D. Soo, J. Xu, Bottom-Up Engineering Strategies for High-Performance Thermoelectric Materials, Nano-Micro Lett. 13(1) (2021) 119.

[25] C. Fiedler, T. Kleinhanns, M. Garcia, S. Lee, M. Calcabrini, M. Ibáñez, Solution-Processed Inorganic Thermoelectric Materials: Opportunities and Challenges, Chem. Mater. 34(19) (2022) 8471-8489.

[26] M. Zubair, V.A. Lebedev, M. Mishra, T.E. Adegoke, I.S. Amiinu, Y. Zhang, A. Cabot, S. Singh, K.M. Ryan, Precursor-Mediated Colloidal Synthesis of Compositionally Tunable Cu–Sb–M–S (M = Zn, Co, and Ni) Nanocrystals and Their Transport Properties, Chem. Mater. 34(23) (2022) 10528–10537.

[27] B. Nan, X. Song, C. Chang, K. Xiao, Y. Zhang, L. Yang, S. Horta, J. Li, K.H. Lim, M. Ibáñez, A. Cabot, Bottom-Up Synthesis of SnTe-Based Thermoelectric Composites, ACS Appl. Mater. Interfaces 15(19) (2023) 23380-23389.

[28] B. Nan, C. Chang, Z. Li, N. Kapuria, X. Han, M. Li, H. Wang, K.M. Ryan, J. Arbiol, A. Cabot, Nanocrystal-based thermoelectric SnTe-$NaSbSe_2$ alloys with strengthened band convergence and reduced thermal conductivity, Chem. Eng. J. (2024) 152367.

[29] N. Kapuria, M. Conroy, V.A. Lebedev, T.E. Adegoke, Y. Zhang, I.S. Amiinu, U. Bangert, A. Cabot, S. Singh, K.M. Ryan, Subsuming the Metal Seed to Transform Binary Metal Chalcogenide Nanocrystals into Multinary Compositions, ACS Nano 16(6) (2022) 8917–8927.

[30] Y. Liu, D. Cadavid, M. Ibáñez, J. De Roo, S. Ortega, O. Dobrozhan, M. V. Kovalenko, A. Cabot, Colloidal $AgSbSe_2$ nanocrystals: surface analysis, electronic doping and processing into thermoelectric nanomaterials, J. Mater. Chem. C 4(21) (2016) 4756-4762.

[31] Y. Liu, G. García, S. Ortega, D. Cadavid, P. Palacios, J. Lu, M. Ibáñez, L. Xi, J. De Roo, A.M. López, S. Martí-Sánchez, I. Cabezas, M.d.l. Mata, Z. Luo, C. Dun, O. Dobrozhan, D.L. Carroll, W. Zhang, J. Martins, M.V. Kovalenko, J. Arbiol, G. Noriega, J. Song, P. Wahnón, A. Cabot, Solution-based synthesis and processing of Sn- and Bi-doped Cu_3SbSe_4 nanocrystals, nanomaterials and ring-shaped thermoelectric generators, J. Mater. Chem. A 5(6) (2017) 2592-2602.

[32] N. Kapuria, B. Nan, T.E. Adegoke, U. Bangert, A. Cabot, S. Singh, K.M. Ryan, Colloidal Synthesis of Multinary Alkali-Metal Chalcogenides Containing Bi and Sb: An Emerging Class of I–V–VI_2 Nanocrystals with Tunable Composition and Interesting Properties, Chem. Mater. 35(12) (2023) 4810–4820.

[33] M. Ibáñez, D. Cadavid, U. Anselmi-Tamburini, R. Zamani, S. Gorsse, W. Li, A.M. López, J.R. Morante, J. Arbiol, A. Cabot, Colloidal synthesis and thermoelectric properties of Cu_2SnSe_3 nanocrystals, J. Mater. Chem. A 1(4) (2013) 1421-1426.

[34] M. Ibáñez, R. Zamani, A. LaLonde, D. Cadavid, W. Li, A. Shavel, J. Arbiol, J.R. Morante, S. Gorsse, G.J.

Snyder, A. Cabot, $Cu_2ZnGeSe_4$ Nanocrystals: Synthesis and Thermoelectric Properties, J. Am. Chem. Soc. 134(9) (2012) 4060-4063.

[35] M. Ibáñez, D. Cadavid, R. Zamani, N. García-Castelló, V. Izquierdo-Roca, W. Li, A. Fairbrother, J.D. Prades, A. Shavel, J. Arbiol, A. Pérez-Rodríguez, J.R. Morante, A. Cabot, Composition Control and Thermoelectric Properties of Quaternary Chalcogenide Nanocrystals: The Case of Stannite $Cu_2CdSnSe_4$, Chem. Mater. 24(3) (2012) 562-570.

[36] W. Li, M. Ibáñez, D. Cadavid, R.R. Zamani, J. Rubio-Garcia, S. Gorsse, J.R. Morante, J. Arbiol, A. Cabot, Colloidal synthesis and functional properties of quaternary Cu-based semiconductors: $Cu_2HgGeSe_4$, J. Nanopart. Res. 16(3) (2014) 2297.

[37] H. Jang, Y.S. Jung, M.-W.J.H. Oh, Advances in thermoelectric AgBiSe2: Properties, strategies, and future challenges, Heliyon 9(11) (2023).

[38] L. Pan, D. Bérardan, N. Dragoe, High Thermoelectric Properties of n-Type $AgBiSe_2$, J. Am. Chem. Soc. 135(13) (2013) 4914-4917.

[39] C. Xiao, X. Qin, J. Zhang, R. An, J. Xu, K. Li, B. Cao, J. Yang, B. Ye, Y. Xie, High Thermoelectric and Reversible p-n-p Conduction Type Switching Integrated in Dimetal Chalcogenide, J. Am. Chem. Soc. 134(44) (2012) 18460-18466.

[40] C. Xiao, J. Xu, B. Cao, K. Li, M. Kong, Y. Xie, Solid-Solutioned Homojunction Nanoplates with Disordered Lattice: A Promising Approach toward "Phonon Glass Electron Crystal" Thermoelectric Materials, J. Am. Chem. Soc. 134(18) (2012) 7971-7977.

[41] T. Bernges, J. Peilstöcker, M. Dutta, S. Ohno, S.P. Culver, K. Biswas, W.G. Zeier, Local Structure and Influence of Sb Substitution on the Structure–Transport Properties in $AgBiSe_2$, Inorg. Chem. 58(14) (2019) 9236-9245.

[42] K. Kravchyk, L. Protesescu, M.I. Bodnarchuk, F. Krumeich, M. Yarema, M. Walter, C. Guntlin, M.V. Kovalenko, Monodisperse and Inorganically Capped Sn and Sn/SnO_2 Nanocrystals for High-Performance Li-Ion Battery Anodes, J. Am. Chem. Soc. 135(11) (2013) 4199-4202.

[43] B.H. Toby, EXPGUI, a graphical user interface for GSAS, J. Appl. Crystallogr. 34(2) (2001) 210-213.

[44] S.A. Vaselabadi, K. Palmer, W.H. Smith, C.A. Wolden, Scalable Synthesis of Selenide Solid-State Electrolytes for Sodium-Ion Batteries, Inorg. Chem. 62(42) (2023) 17102-17114.

[45] M. Dutta, K. Pal, U.V. Waghmare, K. Biswas, Bonding heterogeneity and lone pair induced anharmonicity resulted in ultralow thermal conductivity and promising thermoelectric properties in n-type $AgPbBiSe_3$, Chem. Sci. 10(18) (2019) 4905-4913.

[46] W. Mi, P. Qiu, T. Zhang, Y. Lv, X. Shi, L. Chen, Thermoelectric transport of Se-rich Ag_2Se in normal phases and phase transitions, Appl. Phys. Lett. 104(13) (2014) 133903.

[47] C. Gayner, K.K. Kar, W. Kim, Recent progress and futuristic development of PbSe thermoelectric materials and devices, Mater. Today Energy 9 (2018) 359-376.

[48] P.H. Soni, S.R. Bhavsar, C.F. Desai, G.R. Pandya, Growth and characterization of $InxBi_{2-x}Te_3$ single crystals, J. Cryst. Growth 340(1) (2012) 98-101.

[49] Y.X. Tang, A.J. Hong, W.J. Zhai, Y. Shao, L. Lin, Z.B. Yan, X.H. Zhou, X.M. Lu, C. Chen, X.P. Jiang, J.-M. Liu, Ultralow thermal conductivity of thermoelectric compound Ag2BaGeSe4, AIP Advances 11(12) (2021).

[50] K. Wei, G.S. Nolas, Synthesis and Characterization of Nanostructured Stannite $Cu_2ZnSnSe_4$ and $Ag_2ZnSnSe_4$ for Thermoelectric Applications, ACS Appl. Mater. Interfaces 7(18) (2015) 9752-9757.

[51] Y. Lou, W. Zhao, C. Li, H. Huang, T. Bai, C. Chen, C. Liang, Z. Shi, D. Zhang, X.-B. Chen, S. Feng, Application of $Cu_3InSnSe_5$ Heteronanostructures as Counter Electrodes for Dye-Sensitized Solar Cells, ACS Appl. Mater. Interfaces 9(21) (2017) 18046-18053.

[52] S.N. Guin, V. Srihari, K. Biswas, Promising thermoelectric performance in n-type $AgBiSe_2$: effect of

aliovalent anion doping, J. Mater. Chem. A 3(2) (2015) 648-655.

[53] Y. Liu, M. Li, S. Wan, K.H. Lim, Y. Zhang, M. Li, J. Li, M. Ibáñez, M. Hong, A. Cabot, Surface Chemistry and Band Engineering in $AgSbSe_2$: Toward High Thermoelectric Performance, ACS Nano 17(12) (2023) 11923-11934.

[54] J. Wang, A. Singh, P. Liu, S. Singh, C. Coughlan, Y. Guo, K.M. Ryan, Colloidal Synthesis of Cu_2SnSe_3 Tetrapod Nanocrystals, J. Am. Chem. Soc. 135(21) (2013) 7835-7838.

[55] M. Ibáñez, Z. Luo, A. Genç, L. Piveteau, S. Ortega, D. Cadavid, O. Dobrozhan, Y. Liu, M. Nachtegaal, M. Zebarjadi, J. Arbiol, M.V. Kovalenko, A. Cabot, High-performance thermoelectric nanocomposites from nanocrystal building blocks, Nat. Commun. 7(1) (2016) 10766.

[56] Y. Liu, D. Cadavid, M. Ibáñez, S. Ortega, S. Martí-Sánchez, O. Dobrozhan, M.V. Kovalenko, J. Arbiol, A. Cabot, Thermoelectric properties of semiconductor-metal composites produced by particle blending, APL Mater. 4(10) (2016) 104813.

[57] Y. Zhang, Y. Liu, K.H. Lim, C. Xing, M. Li, T. Zhang, P. Tang, J. Arbiol, J. Llorca, K.M. Ng, M. Ibáñez, P. Guardia, M. Prato, D. Cadavid, A. Cabot, Tin Diselenide Molecular Precursor for Solution-Processable Thermoelectric Materials, Angew.Chem. Int. Ed. 130(52) (2018) 17309-17314.

[58] Z. Guo, Y.-K. Zhu, M. Liu, X. Dong, B. Sun, F. Guo, Q. Zhang, J. Li, W. Gao, Y.-d. Fu, W. Cai, J. Sui, Z. Liu, Cubic phase stabilization and thermoelectric performance optimization in $AgBiSe_2$–SnTe system, Mater. Today Phys. 38 (2023) 101238.

[59] Y. Min, M. Kim, G.-T. Hwang, C.-W. Ahn, J.-J. Choi, B.-D. Hahn, W.-H. Yoon, G.D. Moon, C.-S. Park, C.-H. Park, Vacancy engineering in rock-salt type $(IV\text{-}VI)_x(V\text{-}VI)$ materials for high thermoelectric performance, Nano Energy 78 (2020) 105198.

[60] M. Li, Y. Liu, Y. Zhang, X. Han, K. Xiao, M. Nabahat, J. Arbiol, J. Llorca, M. Ibañez, A. Cabot, PbS–Pb–Cu_xS Composites for Thermoelectric Application, ACS Appl. Mater. Interfaces 13(43) (2021) 51373–51382.

[61] F.A. Kröger, G. Diemer, H.A. Klasens, Nature of an Ohmic Metal-Semiconductor Contact, Phys. Rev. 103(2) (1956) 279-279.

[62] X. Li, Y. Lu, K. Cai, M. Gao, Y. Li, Z. Wang, M. Wu, P. Wei, W. Zhao, Y. Du, S. Shen, Exceptional power factor of flexible Ag/Ag_2Se thermoelectric composite films, Chem. Eng. J. 434 (2022).

[63] E. Rathore, S.N. Guin, K. Biswas, Enhancement of thermoelectric performance of *n*-type $AgBi_{1+x}Se_2$ via improvement of the carrier mobility by modulation doping, Bull. Mater. Sci. 43(1) (2020) 315.

[64] W. Wang, D. Shen, H. Li, C. Chen, Y. Chen, Thermoelectric Optimization of n-Type $AgBiSe_2$ via Se Vacancy Control and Transition-Metal Doping, ACS Appl. Energy Mater. 6(18) (2023) 9709–9715.

[65] Y. Hu, S. Yuan, H. Huo, J. Xing, K. Guo, X. Yang, J. Luo, G.-H. Rao, J.-T. Zhao, Stabilized cubic phase $BiAgSe_{2-x}S_x$ with excellent thermoelectric properties via phase boundary engineering, J. Mater. Chem. C 9(21) (2021) 6766-6772.

[66] J. Dong, D. Zhang, J. Liu, Y. Jiang, X.Y. Tan, N. Jia, J. Cao, A. Suwardi, Q. Zhu, J. Xu, J.-F. Li, Q. Yan, N-Type Thermoelectric $AgBiPbS_3$ with Nanoprecipitates and Low Thermal Conductivity, Inorg. Chem. 62(43) (2023) 17905-17912.

[67] Y. Wu, X. Su, D. Yang, Q. Zhang, X. Tang, Boosting Thermoelectric Properties of $AgBi_3(Se_yS_{1-y})_5$ Solid Solution via Entropy Engineering, ACS Appl. Mater. Interfaces 13(3) (2021) 4185-4191.

[68] T. Zhao, H. Zhu, B. Zhang, S. Zheng, N. Li, G. Wang, G. Wang, X. Lu, X. Zhou, High thermoelectric performance of tellurium-free n-type $AgBi_{1-x}Sb_xSe_2$ with stable cubic structure enabled by entropy engineering, Acta Mater. 220 (2021) 117291.

[69] Y. Wei, Z. Ma, W. Li, C. Li, B. Yang, C. Sun, S. Gang, W. Zhang, H. Long, X. Li, Q. Jiang, D. Zhang, Y. Luo, J. Yang, A New N-Type High Entropy Semiconductor $AgBiPbSe_2S$ with High Thermoelectric and Mechanical Properties, Adv. Funct. Mater. (2024) 2313719.

[70] W. Huang, Y. Zhu, Y. Liu, S. Tao, C. Yang, Q. Diao, Z. Hong, H. Han, L. Liu, W. Xu, Long-range ordering and local structural disordering of $BiAgSe_2$ and BiAgSeTe thermoelectrics, Phys. Chem. Chem. Phys. 23(42) (2021) 24328-24335.

[71] X. Bao, S. Hou, Z. Wu, X. Wang, L. Yin, Y. Liu, H. He, S. Duan, B. Wang, J. Mao, F. Cao, Q. Zhang, Mechanical properties of thermoelectric generators, J. Mater. Sci. Technol. 148 (2023) 64-74.

[72] Q. Yan, M.G. Kanatzidis, High-performance thermoelectrics and challenges for practical devices, Nat. Mater. 21(5) (2022) 503-513.

[73] Y.-K. Zhu, Y. Sun, J. Zhu, K. Song, Z. Liu, M. Liu, M. Guo, X. Dong, F. Guo, X. Tan, B. Yu, W. Cai, J. Jiang, J. Sui, Mediating Point Defects Endows n-Type Bi_2Te_3 with High Thermoelectric Performance and Superior Mechanical Robustness for Power Generation Application, Small 18(23) (2022) 2201352.

[74] H. Wang, G. Han, B. Zhang, Y. Chen, X. Liu, K. Zhang, X. Lu, G. Wang, X. Zhou, $AgSbSe_2$ Inclusions Enabling High Thermoelectric and Mechanical Performance in n-Type Ag_2Se-based Composites, Acta Mater. 248 (2023) 118753.

[75] Q. Jiang, S. Li, Y. Luo, J. Xin, S. Li, W. Li, G. Zhao, J. Yang, Ecofriendly Highly Robust Ag_8SiSe_6-Based Thermoelectric Composites with Excellent Performance Near Room Temperature, ACS Appl. Mater. Interfaces 12(49) (2020) 54653-54661.

[76] H. Wang, C. Tan, A. Romanenko, Y. Sun, J. Feng, M. Khan, G. Chebanova, L. Wang, J. Yao, H. Wang, C. Wang, Crystal structure modulation of SnSe thermoelectric material by $AgBiSe_2$ solid solution, J. Eur. Ceram. Soc. 43(8) (2023) 3383-3389.

[77] L.-Y. Lou, J. Yang, Y.-K. Zhu, H. Liang, Y.-X. Zhang, J. Feng, J. He, Z.-H. Ge, L.-D. Zhao, Tunable Electrical Conductivity and Simultaneously Enhanced Thermoelectric and Mechanical Properties in n-type $B_{i2}Te_3$, Adv. Sci. 9(27) (2022) 2203250.

[78] S.N. Guin, K. Biswas, Cation Disorder and Bond Anharmonicity Optimize the Thermoelectric Properties in Kinetically Stabilized Rocksalt $AgBiS_2$ Nanocrystals, Chem. Mater. 25(15) (2013) 3225-3231.

[79] J. Arbiol, R. Ciancio, R.E. Dunin-Borkowski, R. Holmestad, A.I. Kirkland, M. Kociak, G. Kothleitner, E. Snoeck, J. Verbeeck, e-DREAM: the European Distributed Research Infrastructure for Advanced Electron Microscopy, Microsc. Microanal. 28(S1) (2022) 2900-2902.

Highlights

1. Quaternary $Ag_2SbBiSe_4$ NCs are synthesized by a colloidal synthesis route.
2. $Ag_2SbBiSe_4$ has a cubic crystal structure and a wide band gap.
3. $Ag_2SbBiSe_4$ maintains low lattice thermal conductivity of ca. 0.34 W $m^{-1}K^{-1}$.
4. Modulation doping through Sn NCs is used to tune the TE performance of $Ag_2SbBiSe_4$.
5. A maximum *ZT* value of 0.64 at 760 K are achieved.
6. A high Vickers Hardness of ~185 Hv is obtained.